HAL open science

Effect of magnetic nozzle geometry on ion and electron properties

Alfio E Vinci, Stéphane Mazouffre

To cite this version:

Alfio E Vinci, Stéphane Mazouffre. Effect of magnetic nozzle geometry on ion and electron properties. 73rd International Astronautical Congress, Sep 2022, Paris, France. hal-03797523

HAL Id: hal-03797523

https://hal.science/hal-03797523v1

Submitted on 10 Oct 2022

HAL is a multi-disciplinary open access archive for the deposit and dissemination of scientific research documents, whether they are published or not. The documents may come from teaching and research institutions in France or abroad, or from public or private research centers.

L'archive ouverte pluridisciplinaire **HAL**, est destinée au dépôt et à la diffusion de documents scientifiques de niveau recherche, publiés ou non, émanant des établissements d'enseignement et de recherche français ou étrangers, des laboratoires publics ou privés.

Effect of magnetic nozzle geometry on ion and electron properties

Alfio E. Vinci[a]*, Stéphane Mazouffre[b]

[a] *ICARE, CNRS, 1C Avenue de la Recherche Scientifique, 45071 Orléans, France*, alfio.vinci@cnrs-orleans.fr
[b] *ICARE, CNRS, 1C Avenue de la Recherche Scientifique, 45071 Orléans, France*, stephane.mazouffre@cnrs-orleans.fr
* Corresponding Author

Abstract

Ion and electron properties are measured in a helicon plasma source to characterize the plume when the magnetic nozzle throat is axially shifted with respect to the antenna center and to study the electron cooling rate along the magnetic streamlines as the magnetic nozzle divergence is varied. Larger ion currents and increased plasma confinement are achieved when the throat of the magnetic nozzle is located downstream the antenna center, at a distance that equals or exceeds two times the antenna length. Furthermore, the electrons polytropic index shows dissimilar values along distinct streamlines. It is suggested that ionization phenomena and reduced cross-field transport are responsible for departure from adiabatic conditions.

Keywords: magnetic nozzle, electrodeless, helicon plasma, rf

1. Introduction

A recent keen interest in novel electric propulsion technologies stems from an increasing number of small satellites being deployed for plural applications [1–5]. Simple and compact thrusters might enable in-space maneuvering of such small spacecrafts [6]. In this framework, electrodeless plasma thrusters can offer certain advantages compared to consolidated systems. Qualities like a current-free nature, the elimination of plasma-electrodes interaction, the design simplicity, are the asset of this technology which can nominally operate without a dedicated neutralizer and on virtually any propellant. Several research groups are currently involved in experimental [7–12] and numerical [13–15] studies in order to deepen the physical understanding of this technology with the primary aim of improving its propulsive performance.

Most of electrodeless devices, e.g. helicon plasma thrusters (HPT) and electron cyclotron resonance thrusters (ECRT), integrate a magnetic nozzle (MN), which essentially is an externally applied magnetic field that enables transport and acceleration of ions up to supersonic speeds. A number of transport phenomena are seen to occur in a MN as the result of inlet thermal energy usually stored in the electron population, such as an ambipolar diffusion [16] and an azimuthal diamagnetic electron current [17]. Both of them act in converting the electron energy in ion kinetic energy, the former as an electrostatic force term and the latter as an electromagnetic contribution. As a result, the shape of the MN and the location of the throat can strongly impact the device efficiency. Although many aspects of physics involved are understood by now, information about plasma properties recorded in a MN having different geometries can suggest novel approaches to improve propulsive performance.

This paper reports on experimental results obtained in a helicon plasma source operating under several configurations of the external magnetic field. Two separated experimental campaigns are presented through which plasma properties are spatially resolved. The first analysis deals with the characterization of the plasma plume as the location of the magnetic throat is moved with respect to the antenna axial position. The second analysis reports on 2-D measurements of the electron cooling rate retrieved along the magnetic streamlines in three different magnetic nozzle shapes. A detailed description of the experimental setup is provided in Section 2, which includes the helicon source and the diagnostics. Results are presented and discussed in Section 3. Eventually, conclusions are drawn in Section 4.

2. Experimental apparatus

2.1 Helicon plasma source

Measurements of plasma properties are performed in a helicon plasma source, whose main characteristics have been reported in [11, 12, 18]. It is schematically shown in Figure 1.

The tube constituting the discharge chamber is made in borosilicate glass with $\phi = 9.4$ cm inner diameter and $L = 55$ cm length. The origin of the axial coordinate z is arbitrarily defined to coincide with the tube open boundary. Propellant gas is introduced off-axis at the injection plate of the reactor which is placed at the top aper-

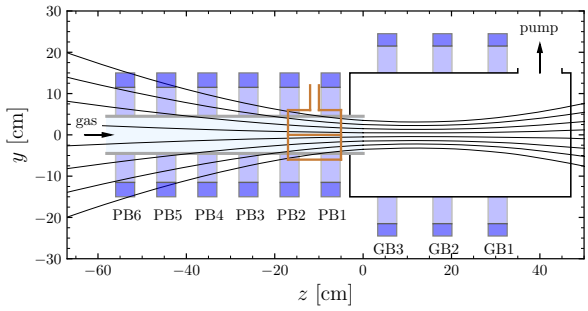

Fig. 1. Helicon source schematics. The $z = 0$ position refers to the discharge tube outlet, $y = 0$ refers to the reactor axis.

ture of the glass tube. The gas goes through a plenum first and eventually reaches the discharge chamber via a multi-perforated plate, resulting in a axial gas flow. The tube is connected to a 30 cm in inner diameter and 50 cm in length expansion chamber made in aluminum which is equipped with a turbomolecular/primary pumping system. The ultimate base pressure is in the order of 1×10^{-5} mbar, whereas the typical pressure during operation reads about 1×10^{-3} mbar.

The rf antenna in use is a double-saddle type with 12 cm length centered at $z \simeq -11$ cm. It is made of pure copper and is directly connected to a custom π-type matching network. Input rf power is generated by a 1 kW-class commercial power supply at 13.56 MHz. Matching of the rf power is manually attained and the reflected power is typically below 1 % during operation. The helicon-mode regime has been experimentally verified in [18] for typical operating conditions.

The plasma source comprises nine electromagnets, six of which surround the discharge tube while three are placed around the expansion chamber, cf. Figure 1. Specifications on the magnetic field used for the presented experiments are provided hereafter within the respective sections.

2.2 Diagnostics

RF-compensated Langmuir probe

Local plasma parameters are measured using the rf-compensated Langmuir probe (RFCLP). A comprehensive technical description of the probe is reported in [18]. The probe design is based on the results and guidelines reported in [19]. The tip of the probe is a 0.38 mm diameter and 5 mm tungsten wire. An additional compensating electrode made of stainless steel is connected in parallel to the tip through a 1 nF axial capacitor and it provides mechanical support to the whole assembly as well. A series of three axial chokes, each of which self-resonates at one of the first three harmonics, ensures the proper rf compensation of the probe [18]. The whole assembly is encapsulated inside a borosilicate glass tube of 6 mm outer diameter, which also accommodates the coaxial cable for probe biasing and current measuring.

I-V curves are recorded using an Automated Langmuir Probe control unit by Impedans Ltd. Eventually, plasma parameters are deduced using the orbital motion limited (OML) theory [20, 21]. Assuming the plasma is locally quasi-neutral, the plasma density n_p is retrieved from the linear fit of the ion current squared versus the probe bias potential. Then, the electron current is computed by subtracting the ion current fit from the total probe current. Under the assumption of a Maxwell-Boltzmann electron distribution function, the electron temperature T_e is inferred from the linear fit of the electron current logarithmic profile versus the probe bias potential. The plasma potential V_p is computed as the probe bias voltage where the first derivative of the I–V curve features its peak value.

The probe is manually actuated within the measurement region using a single-axis translation stage with a resolution of 10 µm and a stroke of 150 mm. The probe is aligned by means of a cross-line laser pendulum.

Planar probe with guard ring

The ion current density j_i is measured using a planar probe with a guard ring (PPGR). It mainly comprises a disk-shaped collector and an outer ring, both made in stainless steel. The role of the guard ring is to concentrate sheath edge effects far from the collector, thus ensuring that the ion collection area exactly corresponds to the collector geometrical area [22]. The collector is 5.6 mm in diameter and 1 mm in thickness, whereas the ring width is 1 mm. A gap of 100 µm is maintained between the two electrodes to ensure electrical insulation. Each electrode features a separated electrical connection for polarization and current measurement. Voltage is applied to the collector by way of a Keithley 2410 SourceMeter, which is also used to measure the flowing current. The guard ring is biased using a TTIEX752M power supply. The probe is manually actuated from outside the chamber using the same single-axis translation stage described in regard of the RFCLP.

3. Experiments, Results and Discussion

The present section details the experimental conditions and the relative results of two separated studies, respectively performed to investigate: *i*) how the magnetic throat location affects the plume properties; *ii*) how the MN divergence impacts the electron thermodynamics. The following sections separately address the two experimental campaigns.

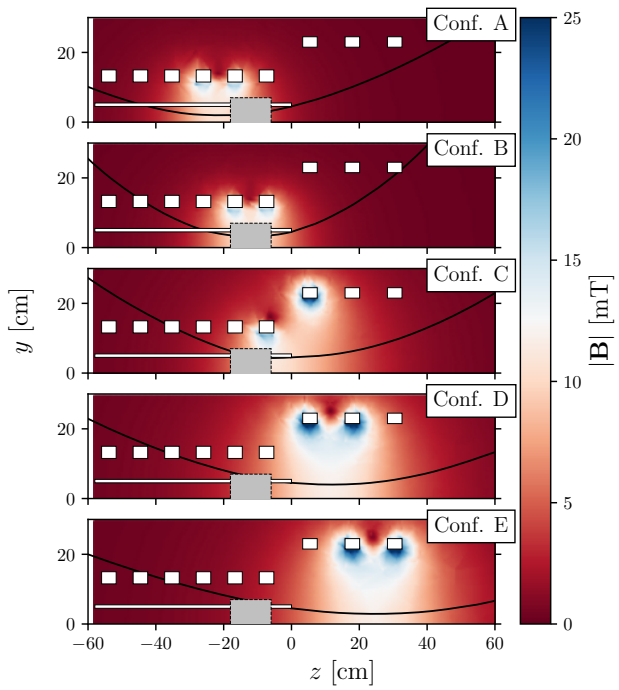

Fig. 2. 2D maps of the external magnetic field. White line indicates the discharge tube walls, white rectangles represent the magnetic coils, the gray rectangle indicates the antenna region and the black solid line exemplifies the magnetic streamline crossing the tube edge at $z = 0$.

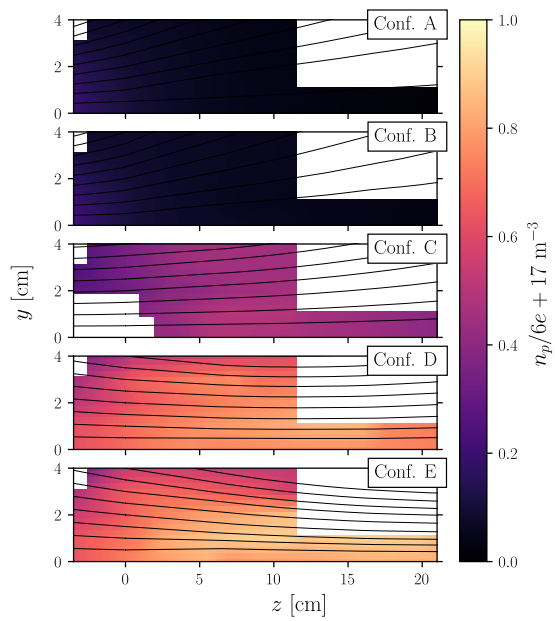

Fig. 3. Normalized plasma density for the five magnetic configurations. Normalization factor is 6×10^{17} m^{-3}. Solid black lines represent magnetic streamlines.

3.1 Effect of the magnetic throat location

For the purpose of this study, the plasma source is operated at 750 W and 1 mg s^{-1} Kr. Five magnetic configurations are examined, each of which is obtained by powering two electromagnets at once so that the location of the magnetic throat is intentionally relocated along the z axis. The tested magnetic configurations are progressively labeled as Conf. A to Conf. E. When involved, PB coils are powered with 3 A and GB coils with 6 A of direct current. Figure 2 shows the computed 2D magnetic field maps, highlighting the streamline that crosses the discharge tube edge at $z = 0$, thus defining the ideal shape of the plasma plume (whether it is assumed fully magnetized). With reference to Figure 2, it is noteworthy to emphasize on the magnetic throat location. It moves from upstream the antenna in Conf. A to far downstream the antenna in Conf. E. The first axial mode the antenna can generate translates in an axial wavelength as $\lambda_z = 24$ cm. Notice that the magnetic throat in Conf. D is approximately one wavelength downstream of the antenna center. All magnetic configurations feature a peak value of about 11 mT with a similar qualitative profile but shifted along z.

Plasma properties are characterized in the region $0 < y < 4$ cm and $-4 < z < 21$ cm with a spatial resolution of 5 mm using the RFCLP described in Section 2.2. Figures 3, 4 and 5 illustrate normalized 2D maps of n_p, T_e and V_p, respectively, for the five magnetic topologies. The solid black lines included in the figures represent the magnetic streamlines delimited by the discharge tube edge at $z = 0$. These experimental measurements show that:

1. when the HP source operates in Conf. A, the extracted plasma plume is characterized by a low monotonically decreasing profile of n_p ranging between $\sim 1 \times 10^{17}$ and $\sim 9 \times 10^{15}$ m^{-3} along the reactor axis. The profile of T_e features a monotonic behavior as well, with a peak value of ~ 3 eV. In a similar fashion, V_p drops from ~ 24 V to ~ 15 V. All plasma properties peak on-axis at $z < 0$. Visual check of the plasma reveals that light is concentrated within the discharge tube. This suggests that the radial and back boundaries represent a major loss term of plasma [23, 24].

2. when the HP source operates in Conf. B, analogous arguments can be put forward. The profile of n_p likewise peaks on-axis at $z < 0$ and decays monotonically downstream. Altogether, slightly larger values of n_p are measured with respect to Conf. A. In the bulk of the plasma, T_e remains in the order of ~ 3 eV

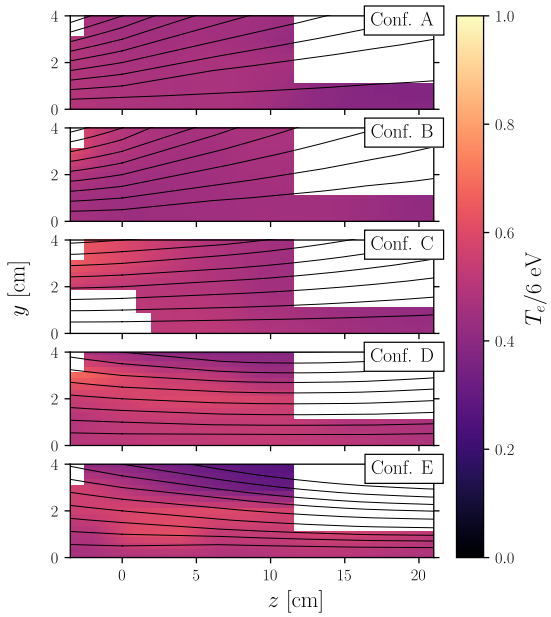

Fig. 4. Normalized electron temperature for the five magnetic configurations. Normalization factor is 6 eV. Solid black lines represent magnetic streamlines.

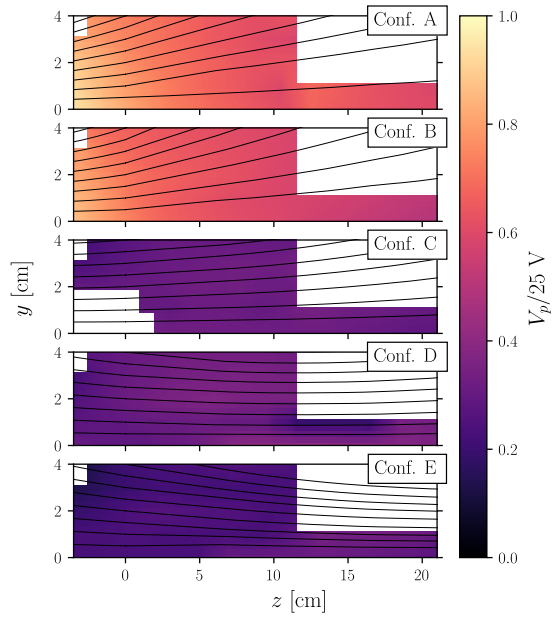

Fig. 5. Normalized plasma potential for the five magnetic configurations. Normalization factor is 25 V. Solid black lines represent magnetic streamlines.

with lower values downstream. However, a population of relatively more energetic electrons ($T_e \sim 3.5$ eV) appears off-axis, in correspondence of the magnetic nozzle edge, visible at $z < 0$ in Figure 4(b). Although qualitatively very similar, the distribution of V_p for Conf. B presents lower values with respect to Conf. A of a few volts.

3. when the HP source operates in Conf. C, results similar to those previously reported in [18] using the same HP source are obtained. As a matter of fact, in both the experiments the magnetic throat is located at $z = 0$. In contrast to what was discussed in points (1) and (2), all plasma properties peak off-axis. Data acquisition in the region ($0 < r < 2$, $z < 0$) was not possible due to discharge instability possibly induced by the probe presence. The largest value of n_p is recorded at $z > 0$ and it reads $\sim 3 \times 10^{17}$ m^{-3}, whereas T_e reaches a peak of 4 eV at $z < 0$. The distribution of V_p is relatively isotropic, ranging in the 8.0(5) V interval. The reason why n_p and T_e present separated regions of the respective maximum values has been explained in [18, 25] in terms of pressure balance.

4. when the HP source operates in Conf. D, light emission upstream the antenna is almost absent, hinting that plasma losses at the back and lateral walls are mitigated with respect to the previous cases. With reference to Figure 3(d), it is evident that n_p follows the axial gradient of B_z. The maximum value of $\sim 5 \times 10^{17}$ m^{-3} is therefore located in correspondence of the magnetic throat. In Figure 4(d), it is relevant to notice the distinct transport pattern of a relatively more energetic electron population along the magnetic field lines at the edge of the nozzle, which exhibits $T_e \approx 3.5 \div 4.2$ eV. A relatively small V_p is measured throughout the probed region, with a peak value in the order of 10 V in the area of maximum n_p.

5. when the HP source operates in Conf. E, similar observations to those stated in point (4) can be raised. Profiles of n_p and T_e have a strong dependence on the spatial distribution of B_r and B_z. The highest plasma density value among all the studied magnetic configurations is herein recorded to be $\sim 5.5 \times 10^{17}$ m^{-3} nearby the magnetic throat. As highlighted in point (4), also in this case a more energetic population of electrons is transported along the external surface of the magnetic nozzle, cf. Figure 4(e). At $z \cong 10$ cm, all the electrons with $T_e \gtrsim 3$ eV are concentrated in a radius of about 3 cm.

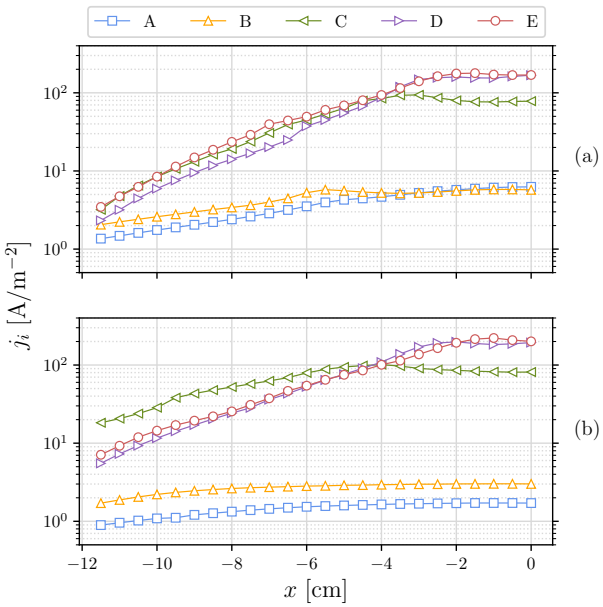

Fig. 6. Ion current density at (a) $z = 5$ and (b) $z = 15$ cm for the five magnetic configurations.

A further insight into the properties of the plasma when operating with the different magnetic topologies is rendered by the employment of the PPGR described in Section 2.2. The probe is displaced radially along the x axis at $z = 5$ cm and $z = 15$ cm in order to analyze the divergence of the extracted plasma plume. The measurements of j_i are shown in Figure 6(a-b). Results confirm that a low-current high-divergence ion beam is extracted from the HP source when operating in Conf. A and B. Differently, the ion beams related to Conf.s C, D and E feature a similar low-divergence profile of j_i in the proximity of the tube exit, see Figure 6(a). Yet, the divergence angle of Conf. C rapidly grows as the plasma expands downstream, cf. Figure 6(b). The highest value of j_i is recorded in Conf.E at $z = 15$ cm, in agreement with the largest n_p probed in the same configuration. Larger values of j_i relate well with higher propellant utilization efficiency, which is a desirable working condition for space propulsion applications.

3.2 *Effect of magnetic nozzle divergence*

In this experiment, the plasma source is operated at 800 W and 0.2 mg s^{-1} Xe. The aim is to retrieve the electron cooling rate along the magnetic streamlines in three different magnetic nozzle shapes. For this purpose, GB1 and GB3 are solely used to exploit three different divergent shapes of the magnetic nozzle. The current dedicated to GB3, i.e. I_{GB3}, is fixed to +9 A, whereas I_{GB1} is set to 0 A, -1 A and -2 A. A positive (negative) value of the current means that the generated **B** field points along the $+z$ ($-z$) direction. In all of the three studied MNs, the peak value of the axial magnetic field reads 8.6(3) mT in correspondence of GB3 at $z \simeq 8$ cm. Each set of currents generates a different shape of the MN whose divergence increases together with the absolute value of I_{GB1}. The streamlines identifying the tested MNs are represented in Figure 7. Every streamline (SL) is numbered and associated with a color which is used afterward for the interpretation of measurement outcomes. The numbering is also included beside each SL within the plots for the sake of clarity.

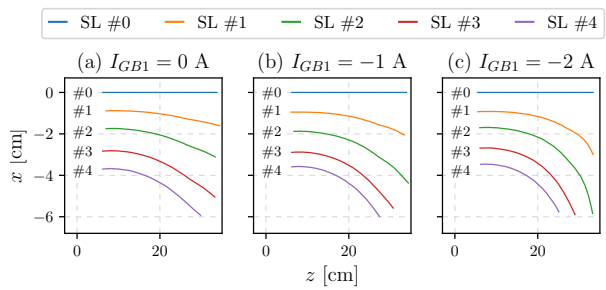

Fig. 7. Magnetic nozzle streamlines for three different cases. The throat is fixed at $z = 8.5$ cm. The nozzle divergence is tuned using different values of I_{GB1}, whereas $I_{GB3} = 9$ A. The color code of the streamlines (SLs) is consistent with that of Figure 10.

For the purpose of studying the electron thermodynamics along the magnetic SLs, the RFCLP is displaced in the region $-6 < x < 0$ cm and $0 < z < 30$ cm to resolve the electron properties. The resulting normalized $(x - z)$ profiles of n_p and T_e are shown in Figure 8 and Figure 9, respectively. The dashed black lines included in each plot reproduce the magnetic SLs as previously displayed in Figure 7. Figure 8 shows that the expanding plasma features a high density region along the HP source axis along with high density conics, which are often observed in other experiments [9, 11, 26]. In the $z < 10$ cm domain, the density increases due to the increasing magnitude of the external magnetic field. Regardless of the MN shape, the highest value of n_p is located off-axis. Yet, the density peak moves upstream as the MN divergence is increased. As a matter of fact, with reference to Figure 8, the maximum of n_p is observed at (a) $z \simeq 17$ cm, (b) $z \simeq 13$ cm and (c) $z \simeq 10$ cm. A positive density gradient beyond the magnetic throat is likely linked to pressure balance effects as analyzed in [18] where the plasma source was operated under similar conditions. Furthermore, the spatial evolution of the high density conics largely resembles the shape of the MN, highlighting that the electrons are visibly magnetized in all of the studied configurations.

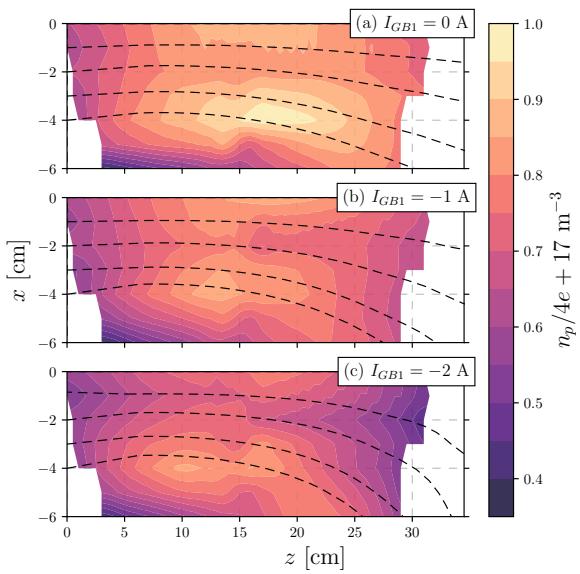

Fig. 8. Contour plots of normalized plasma density for the three tested shapes of the MN. The normalization factor is 4×10^{17} m^{-3}. Dashed black lines represent the magnetic SLs.

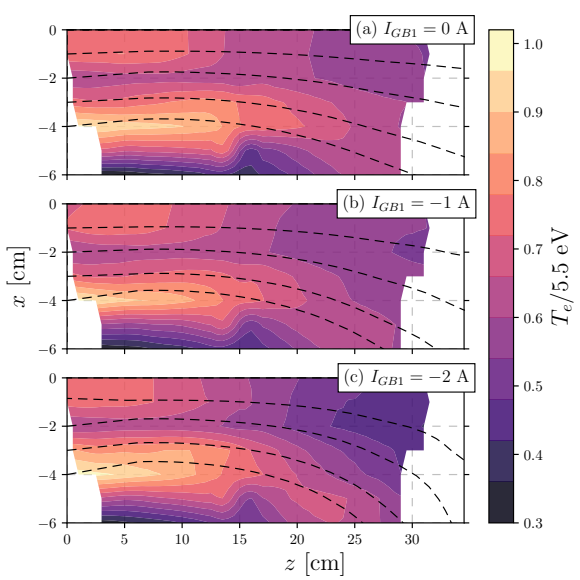

Fig. 9. Contour plots of normalized electron temperature for the three tested shapes of the MN. The normalization factor is 5.5 eV. Dashed black lines represent the magnetic SLs.

Similar comments can be drawn concerning the electron temperature profiles in Figure 9. Relatively higher temperature electrons are localized on-axis and at the external surface of the MN. T_e is larger in the latter region regardless of the MN shape. Some works associate the presence of higher energy electrons at the edge of the MN to heating phenomena near the rf antenna and transport along the SLs [27]. The region at $z \lesssim 10$ cm is visibly unchanged albeit the MN is differently shaped, cf. Figure 9(a-c). It suggests that the discharge process inside the source tube is not deeply influenced by the downstream conditions. At $z > 10$ cm, in contrast, the maps of T_e exhibit important dissimilarities owing to the different shape of the MN. Consistently to what is observed in Figure 8, the spatial evolution of T_e similarly resembles the computed magnetic SLs, further hinting that the electrons are strongly magnetized.

The data mapped in the MN as shown in Figure 8 and Figure 9 is used for analyzing the evolution of the electron flow with a polytropic state equation,

$$T_e/n_p^{\gamma_e - 1} = C(\psi) \tag{1}$$

where γ_e is the polytropic index and C is constant along a characteristic magnetic surface ψ. Note that T_e is in general an effective value of the electron energy. Assuming that the electron inertia is negligible and the electrons are fully magnetized, the magnetic SLs coincide with the electron flow SLs [28]. Hence, the polytropic law is evaluated along the (x,z) coordinates that define the computed magnetic SLs. In order to evaluate (n_p, T_e) at the exact same point $[x,z]$ belonging to the magnetic SL, the experimental maps are numerically interpolated by means of a linear method. Given that n_p increases in the upstream portion of the probed domain, cf. Figure 8, the data of this region is disregarded. In other terms, only the region where $\nabla n_p < 0$ is considered as the focus here is to analyze the expansion process. Eventually, the polytropic index γ_e is inferred using a linear regression of the $\log_{10}(T_e)$ vs. $\log_{10}(n_p)$ datasets. Figure 10 gathers the results obtained evaluating γ_e along the magnetic SLs previously shown in Figure 7 for each of the studied MN shapes. The colors in Figure 10 are consistent with those in Figure 7, thus allowing to identify the magnetic SL that corresponds to each set of scatter points and fitting lines.

Interestingly, γ_e has dissimilar values along distinct SLs. Furthermore, in some cases it reads $\gamma_e > 5/3$ (adiabatic value with $N = 3$ degrees of freedom) and each of the magnetic nozzles being tested features a unique structure of γ_e. In general, γ_e ranges from 1.3 to 1.8. The cases $\gamma_e \simeq 2$ imply that the degrees of freedom of electrons is reduced to 2, while $\gamma_e < 5/3$ would suggest the presence of heat flux within the MN under the hypothesis of local thermodynamic equilibrium (LTE). The study reported in [29] shows that strongly non-Maxwellian EEPF yields an adiabatic expansion with $\gamma_e \simeq 1.17$ in a collisionless regime. However, nearly Maxwellian electrons are found in the

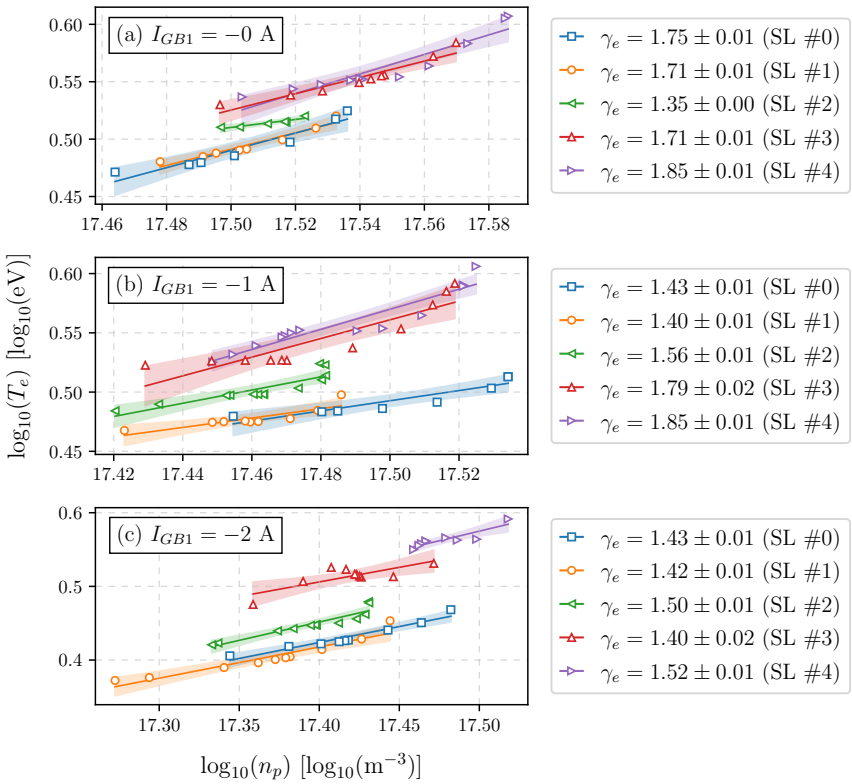

Fig. 10. Electron cooling rate evaluated along the magnetic streamlines for three different magnetic nozzle shapes (a)-(c). The color code relates to Figure 7 to identify the SL corresponding to each dataset. Scatter points represent the interpolated experimental data. Solid lines are the least square linear regressions used to compute γ_e. Colored areas render the 95 % confidence interval of the Student's t-distribution.

present experiment thereby collisionless phenomena are not of primary relevance here. Moreover, the theory developed in [30] fails to predict the values of γ_e observed in this experiment. By using the Spitzer resistivity [31] for the thermal conductivity, the estimation of the Nusselt number based on the experimental data yields $\mathrm{Nu} \sim 10^{-3}$. This would translate into $\gamma_e \approx 1.2$ according to [30] which does not agree with the actual observations. Burm *et al.* [32] suggest that the ionization process serves as an additional degree of freedom in plasma adiabatic expansions. Using the formulation provided in [32] for a monoatomic plasma in non-LTE, i.e. $T_i \neq T_e$ and different ionization degree with respect to Saha equilibrium, the value of γ_e is computed as

$$\gamma_e = \frac{c_p}{c_V} \frac{2\Theta + (1-\Theta)\alpha}{2\Theta + (1-\Theta)\alpha + (1-\alpha)\alpha} \tag{2}$$

where $\Theta = T_i/T_e$ is the ions to electrons temperatures ratio and $\alpha = n_p/n_n$ is the plasma to neutrals density ratio. The expressions for the heat capacity at constant pressure c_p and constant volume c_V are found in [32]. The implementation of this theory yields $\gamma_e \simeq 1.3 - 1.5$ for $T_e = 3 - 6$ eV on the basis that $\Theta \sim 10^{-2}$ and $\alpha \sim 10^{-2}$ in the present experiment. However, the result of Equation 2 is not dramatically affected by small variations in Θ and α compared to the fitting confidence intervals in Figure 10. This means that very dissimilar values of γ_e in this experiment cannot be attributed to small local variations in Θ or α. The value of the polytropic index computed with Equation 2 agrees well with most of the findings shown beforehand in Figure 10. This effectively suggests that ionization within the plume does occur, as previously pointed out in other experiments using a MN [11, 33] and Hall thrusters [34]. Nonetheless, this scenario might not be representative in the far-field region. As collision frequencies drop and α approaches unity, other phenomena besides ionization such as collisionless cooling [35] likely become predominant.

Although the ionization process can clarify the occurrence of $\gamma_e < 5/3$, the physical phenomenon that makes $\gamma_e > 5/3$ has to be investigated. In a simplified picture, the dynamics of electrons in the MN primarily results from

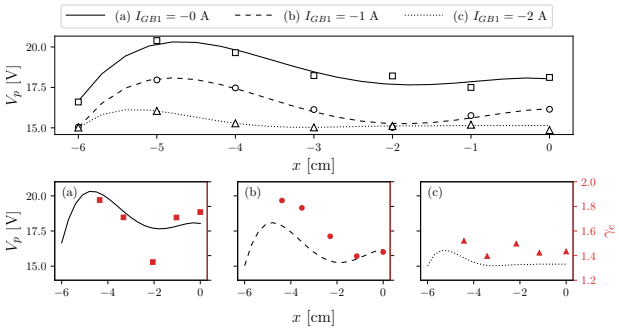

Fig. 11. Radial distribution of plasma potential V_p and polytropic index γ_e at $z = 20$ cm for three different magnetic nozzle shapes (a)-(c). Upper graph: scatter points represent experimental data; lines are computed polynomial fitting curves. Bottom graphs: lines reproduce V_p from the upper plot to enhance visualization (left/black axis); scatter points represent the value of γ_e for each magnetic SL crossing $z = 20$ cm (right/red axis). The bottom graphs share the same scale on the vertical axes for better comparison.

the forces associated with the external magnetic field and the spontaneous electric field. As hinted in [36, 37], the radial electric field in the plasma can profoundly affect the transport across the magnetic lines. In [37], relatively high potential regions concentrated off-axis identify a radial electric field which effectively withdraw the degree of freedom related to the motion perpendicular to **B**. A correlation between the radial V_p and γ_e is therefore quested in the present experiments. The profile of V_p at $z = 20$ cm is retrieved from the measured I-V curves and smoothed as shown in Figure 11(top) for the three shapes of the MN. By determining the radial coordinate where each magnetic SL crosses the section at $z = 20$ cm, the resulting V_p and γ_e radial profiles are compared in Figure 11(bottom). It is found that the two quantities follow a similar qualitative trend along the x axis. As V_p experiences a relatively large variation in the radial direction, so does γ_e, cf. Figure 11(a)-(b). Likewise, a nearly flat profile of V_p produces a small variation in γ_e, as shown in Figure 11(c). At this stage, two points shall be addressed when comparing the studied MNs: (i) the different behavior of γ_e in the proximity of the MN axis; (ii) the relatively large γ_e close to the plasma potential peak. The formulation of a comprehensive theory is beyond the purpose of this paper, hence only a few possible explanations are provided in the following.

A value of $\gamma_e > 5/3$ close to $x = 0$ is found only for the first MN, cf. Figure 11(a). This is possibly linked to a more intense magnetic field considering that $\|\mathbf{B}\| \approx B_z$ spans from about 6 mT in case (a) down to 4 mT in case (c). Differently, an increase in γ_e along with V_p is observed in all cases of Figure 11(bottom), reaching $\gamma_e \simeq 1.7 - 1.9$ in Figure 11(a-b). A larger γ_e where V_p is higher seems at odds with the claims in [36, 37]. In the region where the plasma potential is large, rather than owing to the radial electric field, the cross-field electron transport is more likely reduced because a large conductivity ensues in the direction parallel to **B** which strongly promotes the longitudinal transport. This is supported by considering that T_e is higher where V_p is larger and that the cross-field diffusion coefficient $D_\perp \sim (k_B T_e)^{-1/2}$ [31], therefore $D_\perp$ decreases in the high temperature region. In extension to the results reported in [36, 37], the present findings suggest that the analysis of the electron cooling dynamics in a MN cannot be addressed regardless of the plasma properties radial profiles throughout the nozzle inlet which are in turn linked to the discharge process.

Nevertheless, it must be emphasized that under the hypothesis of a single isotropic electron fluid, the magnetic field cannot directly modify the number of degrees of freedom [38, 39]. The latter are instead determined by the kinetic nature of the dynamics. The presence of the external magnetic field would contribute to the complexity of the species dynamics, i.e. multiple populations, instabilities and anisotropies might arise thus turning the original assumption behind the concept of γ_e unrealistic. These phenomena and their occurrence are still not fully understood, therefore new and more detailed experimental evidence shall be sought.

Ultimately, a comment is due with regards to the boundary conditions of the plasma studied in this experiment. The interaction between the plasma plume and the vacuum chamber is typically unimportant. However, the diameter of the expansion chamber is about twice that of the plasma column in this case. The metallic walls of the chamber represent both a constant zero-potential boundary and a conductive medium within which closure of internal plasma currents can in principle occur. The latter effect might affect the internal plume structure. Furthermore, the plasma may be thermally connected to the relatively cold walls, thus implying the presence of a heat flux towards the system boundaries. In this experiment, plasma properties are intentionally inferred within a relatively small domain away from the chamber walls in order to downplay all of the aforementioned effects. Yet, their quantitative assessment represents a further challenge in the experimental process which definitely deserves future investigation.

4. Conclusions

In summary, the effect of the magnetic nozzle geometry (throat location and divergence degree) on plasma properties is experimentally inferred to establish strategies for thruster design and optimization. It is found that a low-current high-divergence plume is extracted from the plasma source when the magnetic throat is located upstream or in correspondence of the antenna center point. In those cases, the generated plasma mainly remains within the discharge tube and is lost at the radial and back boundaries. Larger ion currents and higher confinement levels are attained when the magnetic throat is located downstream the antenna, namely at a distance at least equal to the wavelength corresponding to the first order axial mode of the helicon wave. Hence, optimization of the plasma generation process in a Helicon thruster would include the separation of the magnetic throat from the antenna location in accordance with the excited helicon wavelength.

Furthermore, analysis of the electron thermodynamics along the magnetic streamlines shows that the simplest scenario describing an electron flow with 3 degrees of freedom does not provide an accurate picture of the plasma expansion. The introduction of the ionization as an additional degree of freedom allows to better predict the value of the polytropic index for some plasma conditions. In general, the electron polytropic index is observed to be inhomogeneous in space, which emphasizes the prevailing complexities of the MN expansion mechanisms. It is observed that a reduced cross-field transport possibly due to a large longitudinal conductivity can effectively reduce the electrons degrees of freedom to 2.

Acknowledgements

This project has received funding from the European Union's Horizon 2020 research and innovation program under grant agreement No 870542 (HelIcon PlasmA Thruster for In-space Applications).

References

[1] I. Levchenko, K. Bazaka, Y. Ding, Y. Raitses, S. Mazouffre, T. Henning, P. J. Klar, S. Shinohara, J. Schein, L. Garrigues, M. Kim, D. Lev, F. Taccogna, R. W. Boswell, C. Charles, H. Koizumi, Y. Shen, C. Scharlemann, M. Keidar, and S. Xu, "Space micropropulsion systems for Cubesats and small satellites: From proximate targets to furthermost frontiers," *Applied Physics Reviews*, vol. 5, no. 1, 2018.

[2] D. Rafalskyi, J. M. Martínez, L. Habl, E. Zorzoli Rossi, P. Proynov, A. Boré, T. Baret, A. Poyet, T. Lafleur, S. Dudin, and A. Aanesland, "In-orbit demonstration of an iodine electric propulsion system," *Nature*, vol. 599, pp. 411–415, 2021.

[3] I. Levchenko, S. Xu, S. Mazouffre, D. Lev, D. Pedrini, D. Goebel, L. Garrigues, F. Taccogna, and K. Bazaka, "Perspectives, frontiers, and new horizons for plasma-based space electric propulsion," *Physics of Plasmas*, vol. 27, no. 2, 2020.

[4] E. Dale, B. Jorns, and A. Gallimore, "Future directions for electric propulsion research," *Aerospace*, vol. 7, no. 9, 2020.

[5] D. Krejci, L. Grimaud, T. Schönherr, V. Hugonnaud, A. Reissner, and B. Seifert, "ENPULSION NANO and MICRO propulsion systems: development and testing," in *AIAA Propulsion and Energy Forum*, 2021.

[6] D. O'Reilly, G. Herdrich, and D. F. Kavanagh, "Electric propulsion methods for small satellites: A review," *Aerospace*, vol. 8, no. 1, 2021.

[7] B. Wachs and B. Jorns, "Background pressure effects on ion dynamics in a low-power magnetic nozzle thruster," *Plasma Sources Science and Technology*, vol. 29, p. 045002, mar 2020.

[8] F. Romano, G. Herdrich, C. Traub, S. Fasoulas, N. Crisp, S. Edmondson, S. Haigh, S. Livadiotti, V. T. A. Oiko, L. A. Sinpetru, K. Smith, J. Becedas, M. Bisgaard, S. Christensen, V. Hanessian, T. K. Jensen, J. Nielsen, M. Sureda, D. Kataria, B. Belkouchi, A. Conte, S. Seminari, O. Road, E. Deimos, S. Systems, and M. Space, "Design, Set-Up, and First Ignition of the RF Helicon-based Plasma Thruster," in *Space Propulsion Conference 2020+1*, no. March, p. 00247, 2021.

[9] K. Takahashi, T. Sugawara, and A. Ando, "Spatial measurement of axial and radial momentum fluxes of a plasma expanding in a magnetic nozzle," *New Journal of Physics*, vol. 22, no. 7, pp. 0–9, 2020.

[10] K. Takahashi, "Magnetic nozzle radiofrequency plasma thruster approaching twenty percent thruster efficiency," *Scientific Reports*, vol. 11, no. 1, pp. 1–12, 2021.

[11] A. E. Vinci and S. Mazouffre, "Plasma properties conditioned by the magnetic throat location in a helicon plasma device," *Journal of Applied Physics*, vol. 130, no. 183301, 2021.

[12] A. E. Vinci, Q. Delavière-Delion, and S. Mazouffre, "Electron thermodynamics along magnetic nozzle lines in a helicon plasma," *Journal of Electric Propulsion*, vol. 1, no. 4, 2022.

[13] M. Magarotto, M. Manente, F. Trezzolani, and D. Pavarin, "Numerical Model of a Helicon Plasma Thruster," *IEEE Transactions on Plasma Science*, pp. 1–10, 2020.

[14] N. Souhair, M. Magarotto, F. Ponti, and D. Pavarin, "Analysis of the plasma transport in numerical simulations of helicon plasma thrusters," *AIP Advances*, vol. 11, no. 115016, 2021.

[15] M. Merino, J. Nuez, and E. Ahedo, "Fluid-kinetic model of a propulsive magnetic nozzle," *Plasma Sources Sci. Technol.*, 2021.

[16] E. Ahedo and M. Merino, "Two-dimensional supersonic plasma acceleration in a magnetic nozzle," *Physics of Plasmas*, vol. 17, no. 7, p. 073501, 2010.

[17] K. Takahashi, A. Chiba, A. Komuro, and A. Ando, "Experimental identification of an azimuthal current in a magnetic nozzle of a radiofrequency plasma thruster," *Plasma Sources Science and Technology*, vol. 25, p. 055011, aug 2016.

[18] A. E. Vinci and S. Mazouffre, "Direct experimental comparison of krypton and xenon discharge properties in the magnetic nozzle of a helicon plasma source," *Physics of Plasmas*, vol. 28, no. 3, p. 033504, 2021.

[19] I. D. Sudit and F. F. Chen, "RF Compensated Probes for High-density Discharges," *Plasma Sources Science and Technology*, vol. 3, no. 2, pp. 162–168, 1994.

[20] F. F. Chen, "Langmuir probes in RF plasma: Surprising validity of OML theory," *Plasma Sources Science and Technology*, vol. 18, no. 3, 2009.

[21] F. F. Chen, "Langmuir probe analysis for high density plasmas," *Physics of Plasmas*, vol. 8, no. 6, pp. 3029–3041, 2001.

[22] S. Mazouffre, G. Largeau, L. Garrigues, C. Boniface, and K. Dannenmayer, "Evaluation of various probe designs for measuring the ion current density in a Hall thruster plume," *35th International Electric Propulsion Conference*, no. 8-12 October, pp. IEPC–2017–336, 2017.

[23] T. Lafleur, "Helicon plasma thruster discharge model," *Physics of Plasmas*, vol. 21, no. 4, p. 043507, 2014.

[24] K. Takahashi and A. Ando, "Enhancement of axial momentum lost to the radial wall by the upstream magnetic field in a helicon source," *Plasma Physics and Controlled Fusion*, vol. 59, no. 5, 2017.

[25] I. D. Sudit and F. F. Chen, "Discharge equilibrium of a helicon plasma," *Plasma Sources Science and Technology*, vol. 5, no. 1, pp. 43–53, 1996.

[26] C. Charles, "High density conics in a magnetically expanding helicon plasma," *Applied Physics Letters*, vol. 96, no. 5, pp. 13–16, 2010.

[27] K. Takahashi, H. Akahoshi, C. Charles, R. W. Boswell, and A. Ando, "High temperature electrons exhausted from rf plasma sources along a magnetic nozzle," *Physics of Plasmas*, vol. 24, no. 8, pp. 0–4, 2017.

[28] M. Merino and E. Ahedo, "Influence of electron and ion thermodynamics on the magnetic nozzle plasma expansion," *IEEE Transactions on Plasma Science*, vol. 43, no. 1, pp. 244–251, 2015.

[29] Y. Zhang, C. Charles, and R. Boswell, "Thermodynamic Study on Plasma Expansion along a Divergent Magnetic Field," *Physical Review Letters*, vol. 116, no. 2, pp. 1–5, 2016.

[30] J. M. Little and E. Y. Choueiri, "Electron Cooling in a Magnetically Expanding Plasma," *Physical Review Letters*, vol. 117, no. 22, pp. 1–5, 2016.

[31] F. F. Chen, *Introduction to Plasma Physics and Controlled Fusion*. 2016.

[32] K. T. Burm, W. J. Goedheer, and D. C. Schram, "The isentropic exponent in plasmas," *Physics of Plasmas*, vol. 6, no. 6, pp. 2622–2627, 1999.

[33] T. A. Collard and B. A. Jorns, "Magnetic nozzle efficiency in a low power inductive plasma source," *Plasma Sources Science and Technology*, vol. 28, p. 105019, oct 2019.

[34] K. Dannenmayer and S. Mazouffre, "Electron flow properties in the far-field plume of a Electron flow properties in the far-field plume of a Hall thruster," *Plasma Sources Sci. Technol.*, vol. 22, no. 035004, 2013.

[35] M. Merino, P. Fajardo, G. Giono, N. Ivchenko, J. T. Gudmundsson, S. Mazouffre, D. Loubère, and K. Dannenmayer, "Collisionless electron cooling in a plasma thruster plume: Experimental validation of a kinetic model," *Plasma Sources Science and Technology*, vol. 29, no. 3, 2020.

[36] K. Takahashi, C. Charles, R. W. Boswell, and A. Ando, "Thermodynamic Analogy for Electrons Interacting with a Magnetic Nozzle," *Physical Review Letters*, vol. 125, no. 16, p. 165001, 2020.

[37] J. Y. Kim, G. Go, Y. S. Hwang, and K. J. Chung, "Dependence of the polytropic index of plasma on magnetic field," *New Journal of Physics*, vol. 23, no. 5, 2021.

[38] J. A. Bittencourt, *Fundamentals of Plasma Physics*. Springer, 2004.

[39] P. M. Bellan, *Fundamentals of plasma physics*. Cambridge University Press, 2006.